

# Fluorescent molecular hydrogen in the Eagle nebula

L. E. Allen,<sup>\*</sup> M. G. Burton, S. D. Ryder,<sup>†</sup> M. C. B. Ashley and J. W. V. Storey

*School of Physics, University of New South Wales, Sydney 2052, Australia*

Accepted 1998 November 11. Received 1998 November 6; in original form 1998 March 25

## ABSTRACT

We used the University of New South Wales Infrared Fabry-Perot (UNSWIRF) to investigate the photodissociation region (PDR) associated with the ‘elephant trunk’ features in the M16 H II region (the Eagle nebula). Images were made in the H<sub>2</sub> 1–0 S(1) and 2–1 S(1) lines at 2.122 and 2.248 μm, respectively, and in the H I Br γ line at 2.166 μm. The trunk-like features have an average H<sub>2</sub> number density of  $\sim 10^4 \text{ cm}^{-3}$  and are irradiated by a far-UV field  $\sim 10^4 \times$  the ambient interstellar value. The H<sub>2</sub> intensity profile across the trunks is consistent with a simple model in which cylindrical columns of gas are illuminated externally, primarily by a direct component (the stars of NGC 6611), with an additional contribution from an isotropic component (scattered light). We find that most of the H<sub>2</sub> emission from the source is consistent with purely fluorescent excitation, however a significant fraction of the H<sub>2</sub> emission ( $\sim 25$  per cent) from the northernmost column shows evidence for ‘collisional fluorescence’, i.e. redistribution of H<sub>2</sub> level populations through collisions. This emission is confined to clumps up to  $\sim 0.01$  pc in diameter, with densities  $\geq 10^5 \text{ cm}^{-3}$ , and perhaps  $> 10^6 \text{ cm}^{-3}$ , filling at most a few per cent of the volume of the trunks. The line intensities and ratios are consistent with steady-state and not time-dependent PDR models.

**Key words:** shock waves – ISM: clouds – ISM: individual: M16 – ISM: molecules – infrared: ISM: lines and bands.

## 1 INTRODUCTION

Understanding the excitation of molecular clouds is central to investigations of the processes associated with star formation. When the radiant energy released from newly formed stars is imparted to the surrounding molecular gas, some of it excites the rotational–vibrational levels of the hydrogen molecule. Observations of near-infrared H<sub>2</sub> emission lines thus play a crucial role in our understanding of the activity in star-forming regions, and the transfer of energy to the cloud from stellar ultraviolet (UV) radiation.

Photodissociation regions (PDRs) are regions where stellar energy is dumped onto the surface layers ( $A_v \leq 10$  mag) of molecular clouds (Tielens & Hollenbach 1985), and are generally found in sites of recent star formation, in reflection nebulae, and in planetary nebulae. When a far-UV (FUV) photon electronically excites an H<sub>2</sub> molecule, the molecule radiatively decays to vibrationally excited states of the ground electronic state ( $\sim 90$  per cent of the time), or to the vibrational continuum (Black & Dalgarno 1976). At low densities the vibrationally excited H<sub>2</sub> radiatively

decays to the ground state, and a fluorescent spectrum is produced with a low ratio ( $\sim 2$ ) of ( $v = 1-0/v = 2-1$ ) S(1) emission. However, at high densities self-shielding brings the H/H<sub>2</sub> dissociation front close ( $A_v < 1$  mag) to the edge of the cloud, where the temperature can reach  $\sim 1000$  K. The line ratio is then elevated above the purely fluorescent value, due to thermalization of the  $v = 1$  level. H<sub>2</sub> vibrational heating can dominate in dense, hot gas behind a shock or in the dense, hot, FUV-illuminated gas at cloud surfaces (Hollenbach 1988).

Previous studies of the near-infrared lines of H<sub>2</sub> in PDRs have been hampered by either poor spectral resolution, poor spatial resolution, or insufficient spatial coverage. Without high spectral resolution, it is difficult to isolate the faint H<sub>2</sub> line emission, typically a few  $\times 10^{-16} \text{ erg s}^{-1} \text{ cm}^{-2} \text{ arcsec}^{-2}$  in face-on PDRs, from the continuum. However, spectroscopy is an inefficient way of determining the morphology of the H<sub>2</sub>-emitting region. Thus high spectral resolution imaging devices, quickly tunable to emission-line and continuum wavelengths, and providing a relatively large field of view ( $> 1$  arcmin) at subarcsecond resolution, are advantageous. Recently we used UNSWIRF, a near-infrared Fabry-Perot imaging spectrometer, to investigate the PDR in the reflection nebula Parsamian 18 (Ryder et al. 1998a), and here we continue our study of PDRs with an investigation of M16. Observations of the H<sub>2</sub>  $v = 1-0$  and  $v = 2-1$  S(1) lines of molecular hydrogen were made in order to map the H<sub>2</sub> emission. Since the

<sup>\*</sup> Present address: Harvard–Smithsonian Center for Astrophysics, 60 Garden Street, Cambridge, MA 02138, USA. E-mail: leallen@cfa.harvard.edu

<sup>†</sup> Present address: Joint Astronomy Centre, 660 N. A’Ohoku Place, Hilo, HI 96720, USA.

( $1-0/2-1$ ) S(1) line ratio is sensitive to the density and radiation field, we can use our images to trace the variation of these parameters within the source. The H I Br  $\gamma$  line was also observed, to investigate the spatial relationship between the molecular and ionized gas.

M16 (the Eagle nebula) is an H II region within the Ser OB1 star-forming complex in the Serpens molecular cloud. The H II region is ionized by the young cluster NGC 6611, which is  $\sim 2$  kpc away from the Sun and contains at least 20 stars of spectral type B0.5 or earlier, including one O5V (Hillenbrand et al. 1993). At a projected distance from the cluster of  $\sim 2$  pc, where the H II region has expanded into surrounding molecular clouds, a striking elephant trunk morphology results. At optical wavelengths these features are silhouettes, brightly outlined in emission, particularly on the edges that face NGC 6611. The ionization structure of this interface between the H II region and the molecular gas has been described by Hester et al. (1996), who showed that the H $\alpha$ , [S II] and [O III] emission profiles are consistent with those predicted from photoionization models of photoevaporative flows.

The outline of this paper is as follows. In the next section, we describe the observations and data reduction. In Section 3, we present line fluxes and intensities, and describe the morphology of the H<sub>2</sub> and Br  $\gamma$  emission. In Section 4, we discuss a simple PDR model for the H<sub>2</sub> emission, explore variations in the  $1-0/2-1$  S(1) line ratio and discuss our results in the context of time-dependent PDRs. A summary of the results is presented in Section 5.

## 2 OBSERVATIONS

UNSWIRF is a 70-mm diameter Queensgate (UK) Ltd etalon with  $R \sim 4000$ , tunable over both the  $H$  and  $K$  windows. When used in conjunction with the wide-field mode of IRIS<sup>1</sup> at the  $f/36$  focus of the Anglo-Australian Telescope, a roughly circular field of 1.6-arcmin diameter at 0.77 arcsec pixel<sup>-1</sup> is produced. Appropriate 1 per cent bandpass filters are used to ensure only a single order of the etalon is seen by the detector. A thorough description of UNSWIRF and its operation can be found in Ryder et al. (1998b).

A finding chart for our observations is shown in Fig. 1, where the UNSWIRF circular field of view is drawn on an image of M16 in the H $\alpha$  line (+continuum). Following the convention of Hester et al. (1996), we refer to the northernmost elephant trunk feature as ‘column I’ and the adjacent feature as ‘column II’. Observations in the H<sub>2</sub>  $1-0$  S(1) and  $2-1$  S(1) lines were obtained on 1996 April 6 and 1997 April 19 UT, and in the H I Br  $\gamma$  line on 1996 April 6 and 1997 April 20. Column I was observed on the first date, and column II on the second.

For the H<sub>2</sub>  $1-0$  S(1) line, we used UNSWIRF to obtain a sequence of five images spanning the peak and separated by  $\sim 2/3$  of the instrumental profile width. For the H<sub>2</sub>  $2-1$  S(1) and H I Br  $\gamma$  lines, we used three images spaced  $\sim 1/2$  of the profile width apart. In each case, another image at 3–4 profile widths from the line centre was obtained in order to sample the continuum. An integration time of 120 s per etalon setting was used, with non-destructive readouts every 5 s. The same exposure sequence was carried out on the sky 5 arcmin west of M16. The procedure was performed once for each of the 2.122 and 2.166  $\mu\text{m}$  observations, once for the 2.248  $\mu\text{m}$  line observation of column I, and twice for the 2.248  $\mu\text{m}$  of column II. Bias subtraction and linearization were performed during readout. The object frames were sky-subtracted, and then flat-fielded using normalized dome flat-fields, using in each case

images at the matching etalon settings. All frames were then registered using field stars. The continuum frames, scaled according to the line/continuum flux ratio measured for the calibrating standard star, were then subtracted from all other images to leave pure line emission in each. Repeated sequences were reduced separately, then averaged together.

The emission-line images were stacked into cubes of increasing etalon spacing (wavelength), so that a Lorentzian profile could be fitted to the (3 or 4) point spectrum at each pixel. Having already fixed the continuum level to be zero, the number of free parameters in the fitting was further reduced by constraining the width of the profile to be the same as that found by fits to high-resolution scans of Krypton calibration lamp lines (2.1165 and 2.2485  $\mu\text{m}$  for the 2.122 and 2.248  $\mu\text{m}$  cubes, respectively), and an Argon line (2.1534  $\mu\text{m}$  for the 2.166  $\mu\text{m}$  cube). The output of the line fitting includes maps of the peak intensity, as well as the interpolated etalon setting corresponding to that peak. To prevent inclusion of pixels with non-physical intensity peaks (i.e. a bad fitting), blanking masks were constructed by requiring that the fitted peak position lies within the range covered by the etalon sequence. Flux calibration and continuum scaling factors were derived from photometry of  $10 \times 1$  s observations of the spectroscopic standard BS 6441 ( $K = 5.18$ ), at the same etalon settings used for M16. Based on repeated observations of standard stars during each night, we estimate there to be an uncertainty in the absolute levels of the flux calibrations of as much as 30 per cent; this is in addition to any errors quoted in the remainder of the paper.

Most of the data reduction and analysis were done using IRAF.<sup>2</sup> Astrometric solutions were obtained by matching the  $\sim 10$  stars in each field with a  $K$ -band mosaic of M16 kindly provided, along with an astrometric solution, by McCaughrean (in preparation). RMS errors in our six-coefficient solutions using ASTROM<sup>3</sup> were 0.1–0.2 arcsec.

## 3 RESULTS

### 3.1 Line fluxes and intensities

Line images of both columns I and II are shown in Fig. 2, for each of the three lines observed. The H<sub>2</sub>  $1-0$  S(1) line is at the top, followed by the H<sub>2</sub>  $2-1$  S(1) line (greyscale) overlaid with contours of the  $1-0$  S(1) emission, and the Br  $\gamma$  line (greyscale), also overlaid with H<sub>2</sub>  $1-0$  contours. The  $2-1$  S(1) and Br  $\gamma$  images have been aligned with the coordinate frames of the  $1-0$  line images. The exciting UV photons originate from NGC 6611, to the north-west (top right).

#### 3.1.1 H<sub>2</sub>

The H<sub>2</sub>  $1-0$  S(1) traces the interface between cold molecular and ionized gas, i.e. the warm surface of the molecular cloud. The strongest emission features are thus on the edges of the cloud facing the ionizing stars. This surface is less complicated in column II than in column I, lending support to the idea that column II is positioned in the foreground relative to most of the ionizing stars, whereas column I is positioned somewhat behind the source of ionizing radiation, and we see emission from more of its surface (Hester et al.

<sup>2</sup> IRAF is distributed by the National Optical Astronomy Observatories, which are operated by the Association of Universities for Research in Astronomy, Inc., under cooperative agreement with the National Science Foundation.

<sup>3</sup> ASTROM is a Starlink task. The Starlink Project is run by CCLRC on behalf of PPARC.

<sup>1</sup> The infrared imager and spectrometer (Allen et al. 1993) uses a  $128 \times 128$  HgCdTe array manufactured by Rockwell International Science Centre, CA.



**Figure 1.** An  $H\alpha$  (+ continuum) image of M16, obtained with the CTIO/Michigan Curtis Schmidt. The stars responsible for exciting the nebula are  $\sim 2$  pc from the elephant trunks, in the top right quadrant of the image. Approximate locations of the fields imaged with UNSWIRF (1.6 arcmin in diameter) are indicated. North is up and east is to the left.

1996). The fainter  $H_2$  2–1 S(1) line emission generally traces that of the 1–0 S(1) line, as expected in a largely fluorescent source.

Total fluxes, tabulated in Table 1, were obtained for each of the two sources by summing the flux within an aperture (of size specified in Table 1).  $H_2$  1–0 S(1) line intensities range from  $0.1\text{--}3 \times 10^{-15}$   $\text{erg s}^{-1} \text{cm}^{-2} \text{arcsec}^{-2}$ , with average values of  $\sim 0.6\text{--}0.7 \times 10^{-15}$   $\text{erg s}^{-1} \text{cm}^{-2} \text{arcsec}^{-2}$ . In Section 4 we show that these numbers are consistent with predictions from PDR theory. Peak intensities, measured in  $3 \times 3$  arcmin<sup>2</sup> apertures, are also listed in Table 1.

### 3.1.2 $Br\gamma$

The two lower panels in Fig. 2 show the  $Br\gamma$  line emission, overlaid with  $H_2$  1–0 contours. In column I, the ionized emission peaks approximately 4 arcmin (5 pixels) north-west of the strongest  $H_2$  emission, towards the ionizing cluster. Assuming that the UV radiation responsible for exciting the  $H_2$ -emitting gas penetrates

the molecular cloud to a depth  $A_V \sim 1$ , and that the distance to M16 is 2 kpc, then the average hydrogen nucleus density is  $n = 2 \times 10^4 \text{cm}^{-3}$ . A similar density is derived at the top of column II.

The total  $Br\gamma$  flux in the head of column II (an area  $13 \times 19$  arcmin<sup>2</sup>) is  $6.7 \times 10^{-13}$   $\text{erg s}^{-1} \text{cm}^{-2}$ . From this, we can calculate the number of  $Br\gamma$  photons and the number of ionizing photons at the head of the column. The total number of ionizing photons emitted by the exciting stars then follows. The number of ionizing photons at the head of column II is  $2.3 \times 10^{46}$  photon  $\text{s}^{-1}$  (with no allowance for extinction), and the total number of ionizing photons emitted by the stars is  $N_{Ly} = 3.7 \times 10^{49}$  photon  $\text{s}^{-1}$ , assuming the column has a projected radius of 0.1 pc as seen by the ionizing stars  $\sim 2$  pc away. Thus the ionizing luminosity is equivalent to  $\sim 2 \times 10^5 L_\odot$ . We compare the measured number of ionizing photons with the expected number made from the theoretical spectral energy distributions of the 20 stars of type B0.5 and earlier in NGC 6611. Integrating the Planck function from  $h\nu = 13.6 \text{eV} \rightarrow \infty$  for those stars gives  $N_{Ly} = 2.9 \times 10^{50}$  photon  $\text{s}^{-1}$ .

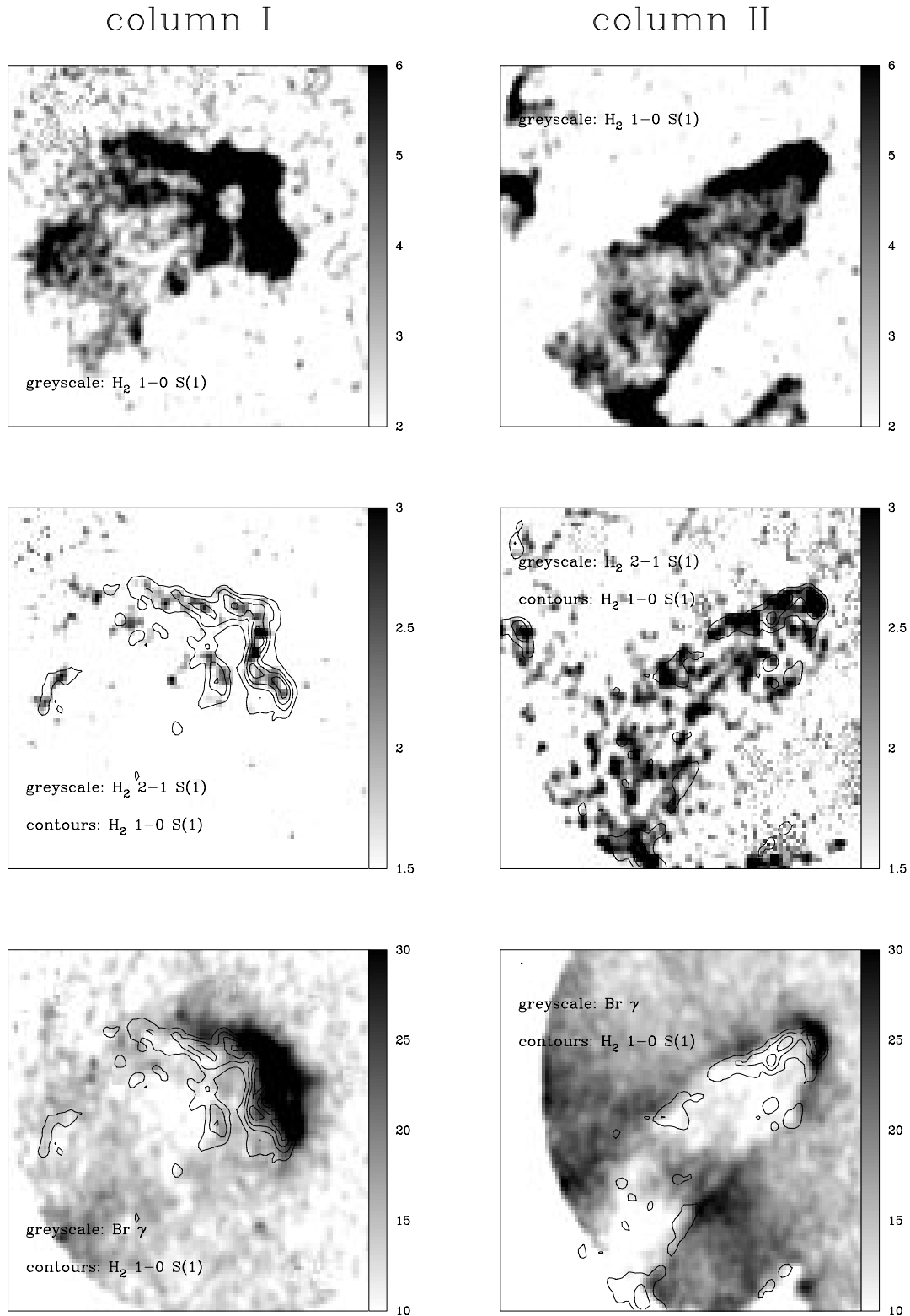


**Figure 2.** Emission-line images in M16. Scale bar shows range of grey-scale, in units of  $10^{-16} \text{ erg s}^{-1} \text{ cm}^{-2} \text{ pixel}^{-1}$ . Contour levels are 6, 10, 14, 18,  $22 \times 10^{-16} \text{ erg s}^{-1} \text{ cm}^{-2} \text{ pixel}^{-1}$ . In all frames north is up and east is to the left. The circular edge of the Fabry-Perot filter appears at the left or lower left of some images.

The discrepancy between the measured and theoretical number of photons is not surprising, given that the Planck function will overestimate the actual UV flux from an early type star. Comparison of a 35 000 K blackbody with a modelled stellar spectrum (Hubeny,

Heap & Lanz 1998) reveals that the Planck function overestimates the Lyman continuum photon rate by about a factor of 2, bringing the theoretical and measured values into closer agreement.

The measured  $\text{Br } \gamma$  flux at the head of column II leads to an

**Table 1.** H<sub>2</sub> and Br  $\gamma$  line fluxes and intensities in M16.

Column	Line	Total flux <sup>a</sup> (erg s <sup>-1</sup> cm <sup>-2</sup> )	Peak intensity <sup>b</sup> (erg s <sup>-1</sup> cm <sup>-2</sup> arcsec <sup>-2</sup> )
I	1-0 S(1)	2.14 ± 0.02(-12)	3.14(-15)
I	2-1 S(1)	4.27 ± 0.18(-13)	4.47(-16)
I	Br $\gamma$	6.46 ± 0.04(-12)	7.53(-15)
II	1-0 S(1)	1.22 ± 0.01(-12)	2.83(-15)
II	2-1 S(1)	7.05 ± 0.15(-13)	7.54(-16)
II	Br $\gamma$	4.84 ± 0.02(-12)	4.56(-15)

<sup>a</sup> Total fluxes measured within a 70 × 70 arcsec<sup>2</sup> aperture in column I and a 60 × 60 arcsec<sup>2</sup> aperture in column II.

<sup>b</sup> Peak intensities measured within a 3 × 3 arcsec<sup>2</sup> aperture.

estimated emission measure of  $1 \times 10^5 \text{ cm}^{-6} \text{ pc}$ . This value is consistent with Hester et al. (1996), who report a value of  $\sim 3 \times 10^5 \text{ cm}^{-6} \text{ pc}$ , after accounting for two magnitudes of extinction at  $V$ .

## 4 DISCUSSION

### 4.1 Geometry

The morphology of the columns suggests that they are dense protrusions of gas, extending from the face of a molecular cloud, and that they have resisted dissociation and ionization in contrast to nebular gas adjacent to them. Molecular hydrogen line emission is co-extensive with the dark silhouettes seen in the optical, and has a morphology quite unlike the hydrogen lines which envelop the columns (Fig. 3). H<sub>2</sub> emission will typically extend one optical depth into a molecular cloud from its surface, the depth to which the FUV photons penetrate and fluoresce the gas. In this section we investigate whether the distribution of the H<sub>2</sub> line emission in the columns is consistent with being excited in cylinders of molecular gas, illuminated externally by a radiation field that has both directed and isotropic components (e.g. from a single dominant star but with scattering and secondary sources important). We then derive some gross physical parameters for the cloud based on the results.

Fig. 4 shows the emission across sections along column II from its head to base. H<sub>2</sub> emission is pervasive across the column, but it is also limb-brightened. In addition the north-east limb is generally brighter than the south-west limb, near the head of the column. We now describe the geometries we have considered in attempting to model these sectional cuts. We stress that these models are descriptive rather than exact, and are designed to understand the overall behaviour rather than specific details. We also have not modelled the emission from the cap at the end of a cylinder, orientated face-on to an illuminating star, although this would be a modest extension of our models.

Consider first an infinitely long cylinder of radius  $R$  (Fig. 5) whose axis is orientated at an angle  $\theta$  in the  $x$ - $z$  plane to an illuminating source along the  $z$ -axis (with  $\theta = 0^\circ$  pointing to the source), and with the observer viewing at angle  $\alpha$  in the  $y$ - $z$  plane ( $\alpha = 90^\circ$  is along the  $y$ -axis, orthogonal to the source).<sup>4</sup> FUV radiation penetrates to  $A_v \sim 1$  into the cylinder, a distance which we vary from  $L = 0$  to  $(2R/\sin\theta)$  (the diameter of the projected ellipse through the cylinder, as seen from the source). This penetration depth depends on the density of the cloud. Physically,  $L$

<sup>4</sup> This is a special case, as in general two angles are required to specify the observer's position, but serves to illustrate the effect of varying the inclination angle of the cylinder.

corresponds to  $\sim 2 \times 10^{21}/n \text{ cm}$ , where  $n$  is the hydrogen number density in  $\text{cm}^{-3}$ . We have assumed that the H<sub>2</sub> line intensity is simply proportional to the distance that a sight line passes through an illuminated section of the cylinder. This, of course, is only an approximation, particularly in the case of dense gas where self-shielding occurs. It also does not incorporate any effects from a clumpy medium, which would result in a varying penetration depth through the cylinder, depending on the spectrum and distribution of clump sizes.

Fig. 6 presents typical results from such a model for a range of penetration depths  $L$ , with  $\theta = 30^\circ$  and  $\alpha = 90^\circ$ . For small  $L$  the emission is strongly limb-brightened, and as  $L$  increases the peak moves into the body of the cylinder. When FUV penetrates most of the cylinder we have a centre-brightened morphology, corresponding to the longest path line through the cylinder. It is clear that limb brightening can readily be modelled with values of  $L$  up to 20–30 per cent of the projected diameter. It cannot, however, replicate limb brightening on both sides of a cylinder. To do so we also consider a contribution from an isotropic radiation field external to the cylinder.

FUV radiation from an external isotropic field will penetrate a depth radially corresponding to  $A_v \sim 1$  into the cylinder. Fig. 7 shows the calculated emission cross-sections for a range of penetration depths up to the cylinder radius. Again limb brightening occurs for depths of up to  $\sim 30$  percent the radius and becomes centrally peaked as we approach 100 per cent. The limb brightening is two-sided and symmetric.

Thus it is clear that a combination of the two radiation fields can produce a range of emission cross-sections, and in particular produce limb brightening with one edge more intense than the other. For a penetration depth of  $\sim 20$  per cent we can produce a cut similar in form to that observed. We now examine the effect of changing the orientation of the cylinder. This makes no difference for an isotropic radiation field, but does significantly change the cross-cuts for radiation incident from a single direction.

Fig. 8 shows some typical results when  $\alpha = 90^\circ$  (i.e. the line of sight is perpendicular to cylinder-source direction), for a range of the angle  $\theta$  between the cylinder axis and the source, when FUV penetrates a distance from the source equal to 20 per cent the radius (this distance is directly away from the source for the directed field and radially inwards towards the cylinder axis for the isotropic field). For a given cloud density the fractional penetration depth along the direction of the long axis of the projected ellipse [the length of which is  $2R/\sin(\theta)$ ] increases with  $\theta$ , and this length has been used to normalize the relative peak intensity between the curves for each value of  $\theta$ . All the cuts are strongly limb-brightened, but the peak is both stronger and moves further into the cylinder as  $\theta$  approaches  $90^\circ$ . We have also investigated varying the line-of-sight to star-cylinder inclination angle  $\alpha$ . Doing so increases the radial extent through the cylinder in which emission occurs, but has little effect on the form of the peak.

Fig. 9 shows a ‘best fitting’, combining an isotropic and a directed radiation field, with  $\theta = 30^\circ$ ,  $\alpha = 90^\circ$  and penetration depth 20 per cent of the cylinder radius. Note we have simply added the intensities produced by the two radiation fields, although in practice they are unlikely to be of equal intensity. However, as is discussed in Section 4.2, when self-shielding is not important, emission intensities are only weakly dependent on the strength of the radiation field. The cylinder radius is 14 pixels or 11 arcsec, which corresponds to  $\sim 0.1 \text{ pc}$ . Thus for a 20 per cent penetration depth it implies that  $n_{\text{H}_2} \sim 10^4 \text{ cm}^{-3}$ , the average density of the gas in the column. This is consistent with the estimate derived from the

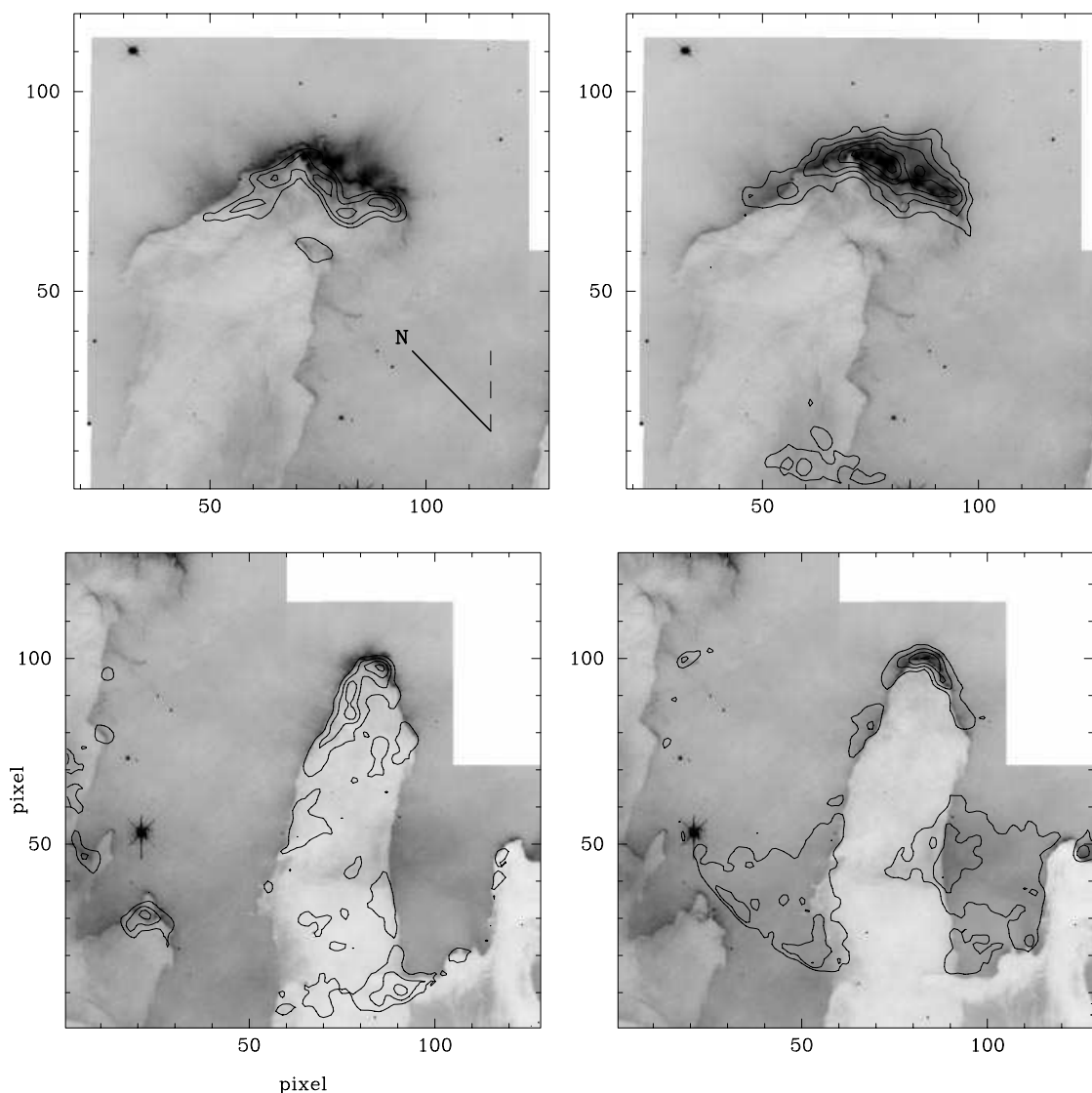


**Figure 3.** Contours of  $\text{H}_2$  1–0 S(1) (left) and  $\text{H Br } \gamma$  (right) line emission overlaid on a greyscale of  $\text{H}\alpha$  line emission imaged by the *Hubble Space Telescope* (Hester et al. 1996), for column I (top) and column II (bottom). The grey-scale is in arbitrary units; the contour levels are approximately the same as in Fig. 2. The images are oriented  $42.2^\circ$  west of north.

separation of the  $\text{Br } \gamma$  and  $\text{H}_2$  peaks at the top of the column (Section 3.1.2). The cylinder is pointing towards the most massive stars in M16, but not straight at them. The  $\text{H}_2$  in it is excited by a radiation field that has two components, one direct from the central stellar cluster, and the other a more isotropic field, presumably a result of multiple scattering of the dissociating photons and from secondary sources distributed throughout M16.

#### 4.2 Line ratios

As noted in Section 3.1.2, the ionizing cluster NGC 6611 contains  $\sim 20$  stars of spectral type B0.5 or earlier distributed over several arcmin on the sky, but the most massive stars in the cluster are located 3.5 arcmin to the north-west of the elephant trunks. Assuming the distance to M16 to be 2 kpc, the exciting stars are at a (projected) distance from the molecular gas columns of approximately 2 pc, and their combined contributions to the local UV field (for photons of energy  $h\nu = 6 - 13.6$  eV) sum to  $15.5 \text{ erg s}^{-1} \text{ cm}^{-2}$ ,

or  $9700 G_0$ , where  $G_0 = 1$  represents the average interstellar radiation field ( $= 1.6 \times 10^{-3} \text{ erg s}^{-1} \text{ cm}^{-2}$ ; Habing 1968).

For gas of density  $n \sim 10^4 \text{ cm}^{-3}$  and FUV radiation field  $G_0 \sim 10^4$ , as inferred above, model predictions (e.g. Burton, Hollenbach & Tielens 1990, hereafter BHT) for the 1–0 S(1) line intensity from a face-on PDR are  $\sim 3 \times 10^{-16} \text{ erg s}^{-1} \text{ cm}^{-2} \text{ arcsec}^{-2}$ . We apply a scaling factor of 3, appropriate for viewing through an excited sheath of  $\sim 20$  per cent the cylinder radius instead of face-on, as inferred from our geometrical modelling of the  $\text{H}_2$  intensity profiles. The resulting line flux is comparable with that of the diffuse flux observed through the columns of gas ( $\sim 6 \times 10^{-16} \text{ erg s}^{-1} \text{ cm}^{-2} \text{ arcsec}^{-2}$ ; Section 3.1.1). These parameters also imply a pure fluorescent value for the 1–0/2–1 S(1) line ratio of  $\sim 1.7$  (Black & Dalgarno 1976; Black & van Dishoeck 1987) as the gas remains below its critical density. While some of the gas indeed has this ratio, the brightest regions typically show a higher line ratio, requiring the existence of dense clumps inside the columns, as we argue below.

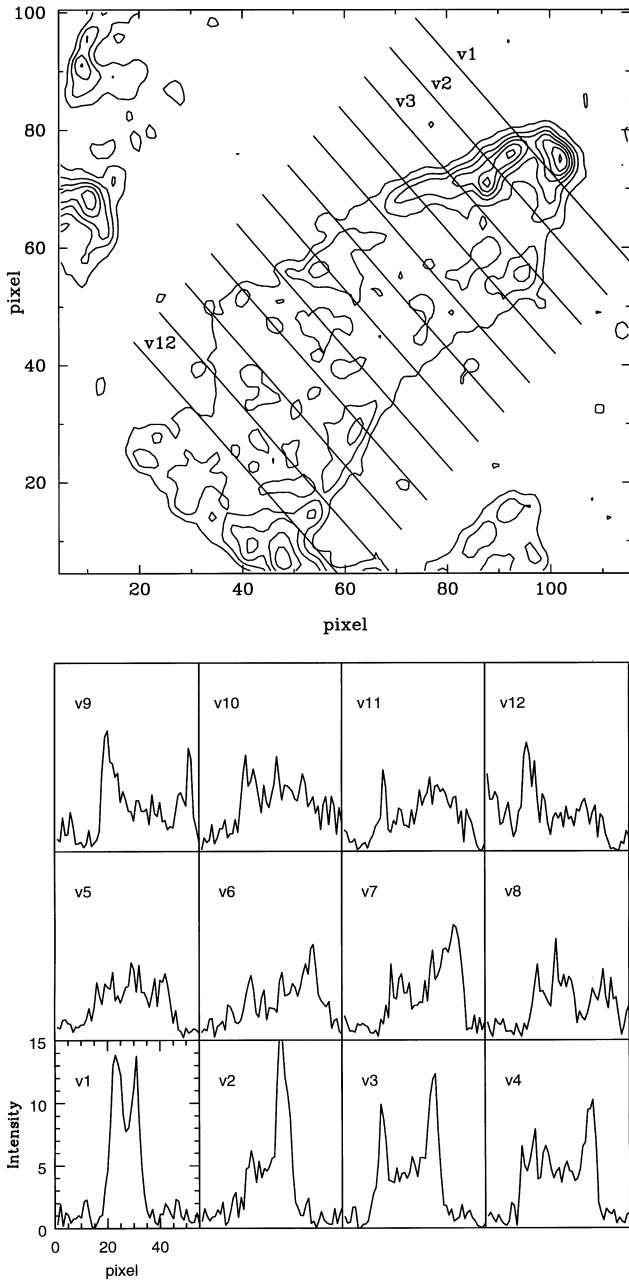


**Figure 4.** Top: locations of cross-sectional cuts of the  $\text{H}_2$  1–0 S(1) image of column II, running SW–NE, every five pixels, from the head to the base. Bottom: plots of intensities are in units of  $10^{-16} \text{ erg s}^{-1} \text{ cm}^{-2} \text{ pixel}^{-1}$ . The image was smoothed with a Gaussian ( $\sigma = 1 \text{ pix}$ ) before the cuts were made.

For a dense PDR, where self-shielding is occurring,  $\text{H}_2$  exists at optical depths  $A_\nu < 1$  from the front surface of the cloud. Then, for a sufficiently strong FUV radiation field, the gas temperature can reach  $\sim 1000 \text{ K}$  or higher, enabling collisions to redistribute the populations in the low- $v$   $\text{H}_2$  energy levels. The (1–0)/(2–1) S(1) line ratio then increases from the pure fluorescent value. It is sensitive to both the density and the strength of the FUV field, and so can be used to constrain these parameters in a source. This is different from shock-excited gas where it has been shown empirically that there is little variation in this line ratio both among and within shocked sources (e.g. Burton et al. 1989). In particular, dense clumps of  $\text{H}_2$  inside the PDRs may have the  $v = 1$  level

thermalized, while being surrounded by lower density gas exhibiting pure fluorescent line ratios. Such clumps would signal their presence by elevated levels of the (1–0)/(2–1) S(1) ratio. This could then be used to probe the structure of the clouds.

The line ratio of the integrated flux in column I is 4.9, and in column II it is 1.7, suggesting that at least some of the gas in column I has been thermalized by the above process. Thus it is useful to examine small regions, and to look for spatial variations in the line ratio. In Fig. 10 we have plotted several measurements of the line ratio as a function of the 1–0 S(1) line intensity. Each point on the graph represents an average value computed for a  $4 \times 4$  pixel region, centred at the marked position in Fig. 11. The boxes were selected to cover a broad range of 1–0 intensities. Many of the line ratios in both columns I and II are elevated relative to the purely fluorescent value, but lie below the ratio expected for shocked gas (Fig. 12). Of note, however, is the difference in distribution of line ratios between the two columns. The average line ratio in the distribution of points measured for column I is 6.6, and for column II, 2.5; thus a higher fraction of the gas in column I must have its pure fluorescent ratios modified by collisions.

Thermalization of the  $v = 1$  level occurs for densities  $\geq 10^5 \text{ cm}^{-3}$ , although significantly elevated 1–0/2–1 S(1) line ratios ( $> 6$ ) do not occur in these models until the density exceeds  $\sim 10^6 \text{ cm}^{-3}$  (e.g. BHT). Virtually all the positions plotted in Fig. 10 for column I show clear evidence for thermalization in the above line ratio (i.e. ratios  $> 3$ ), while approximately 20 per cent do so for column II. For these positions we thus infer densities in excess of  $\sim 10^5 \text{ cm}^{-3}$  and indeed greater than  $10^6 \text{ cm}^{-3}$  for many of those in column I. However, the total intensity in these ‘clumps’ is only about a quarter of the integrated intensity of each column. The pure fluorescent gas still dominates the overall emission, as indeed it must if the modelling in the previous section is to be self-consistent. Column I must have many more dense clumps than column II. However, it is also possible that the FUV field at column II is lower than that at column I if, for instance, it were further away from the exciting stars. This would lower the temperature in the surface layers of column II, reducing the incidence of thermalization and thus the number of dense clumps we could see in it.

Structure in the line ratio map is apparent on 1–2 arcsec scales, and if we assume this size is typical for the clumps we may then infer certain characteristics of the internal structure of the column. The dense clumps are  $\sim 0.01 \text{ pc}$  in diameter, and have a total surface-filling factor of 10 per cent of the projected area of column I and 14 per cent of it for column II. The volume-filling factor of these dense clumps is, however, very small: about a tenth of these values if we assume the clumps are roughly spherical. It is hard to estimate the mass fraction of the columns that is contained in the dense clumps as  $\text{H}_2$  line ratios do not yield accurate density estimates, only the fraction of gas above critical density. However, if all the clumps in column I had a density  $\sim 10^6 \text{ cm}^{-3}$  then there would be roughly equal amounts of molecular gas inside the dense clumps as in the diffuse  $\sim 10^4 \text{ cm}^{-3}$  gas of the column.

Fig. 10 shows that as the 1–0 S(1) line flux increases, the minimum value for the 1–0/2–1 S(1) line ratio also increases. In column II this trend is weak, as the ratio remains close to purely fluorescent, but the effect is marked in column I. If pure fluorescence were occurring, then the line ratio would be constant whatever the intensity: larger intensities simply implying larger filling factors along that sightline. This clearly does not occur. The spread in the line ratio for a fixed 1–0 S(1) line flux, on the other hand, can be understood as a variation in the relative filling factor of low and high density gas in the sightline. The lowest ratio occurs, at

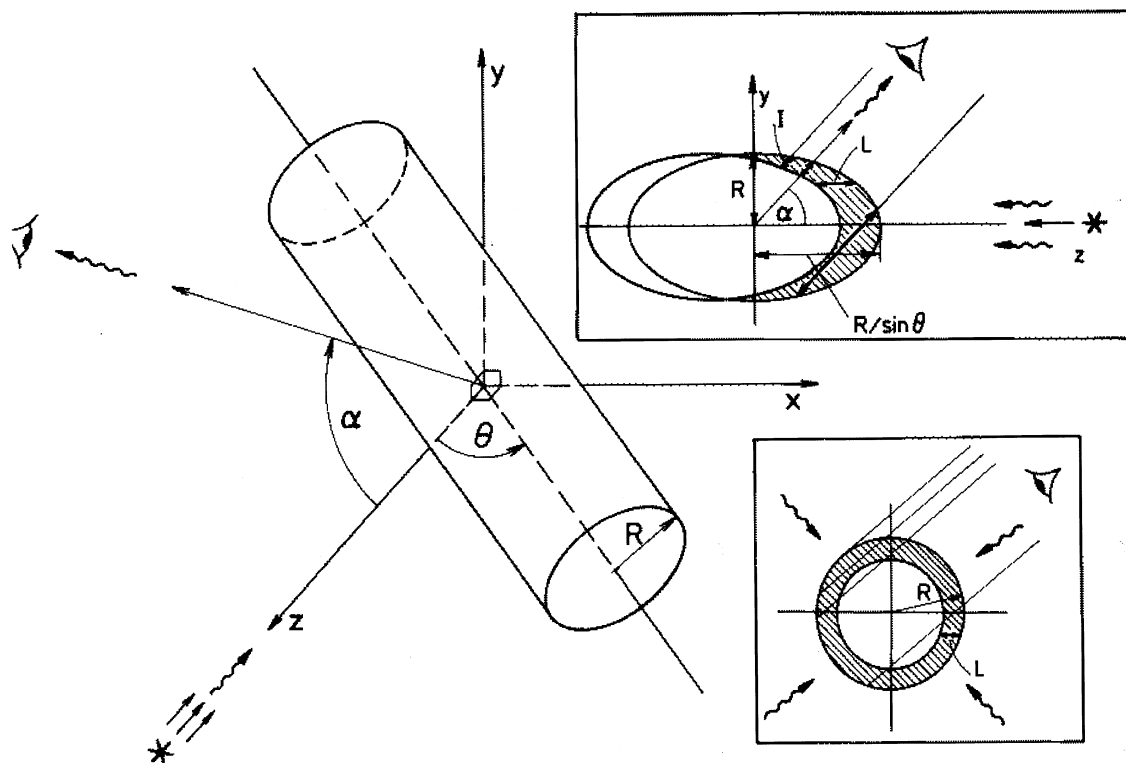


**Figure 5.** A sketch of the geometry of column II, as we have modelled it. The angle between the long axis of the cylinder and the illuminating source is  $\theta$  (in the  $x$ - $z$  plane); the observer is at an angle  $\alpha$  orthogonal to the source-cylinder plane (i.e. in the  $y$ - $z$  plane). FUV radiation is assumed to penetrate a distance  $L$  into the cylinder along the source direction (equivalent to an optical depth of  $A_V \sim 1$ ), producing an emission sheath. The intensity of emission is proportional to the path-length  $l$  from the observer through the emission sheath, as illustrated at top right. The contribution from an isotropic component of the FUV field is illustrated at lower right.

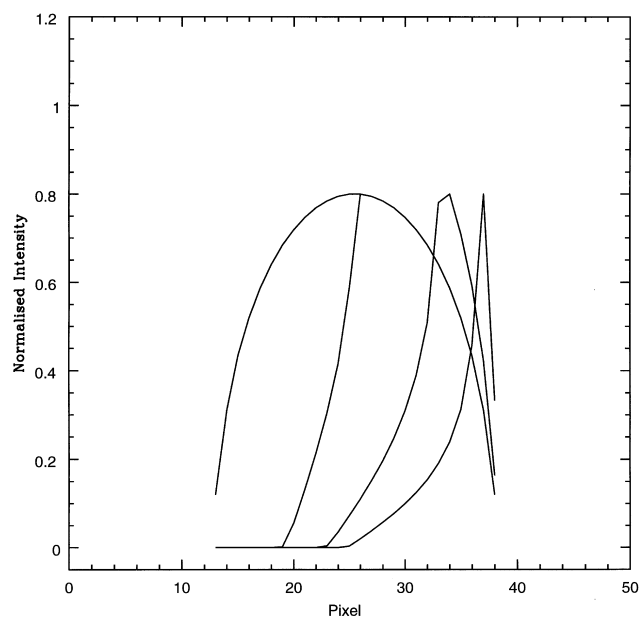


**Figure 6.** Intensity cuts across a model cylinder illuminated by a star orientated at  $\theta = 30^\circ$  to the axis, and viewed orthogonally to the star-cylinder direction ( $\alpha = 90^\circ$ ). The curves correspond to different penetration distances for the FUV radiation into the cloud of (from right to left) 5, 20, 50 and 100 per cent of the projected diameter  $2R/\sin(30^\circ)$ . Spatial resolution is 8 per cent of the radius  $R$ , corresponding to the pixel scale of the data in Fig. 4.

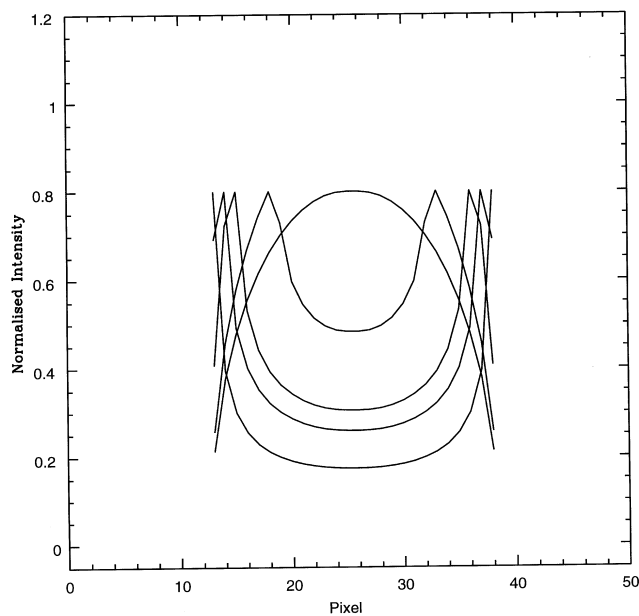


**Figure 7.** Intensity cuts across a model cylinder illuminated isotropically from the outside, with radiation penetrating (from edge to centre) 3, 10, 20, 50 and 100 per cent of the radius  $R$ . Spatial resolution is 8 per cent of  $R$ , as per Fig. 6.

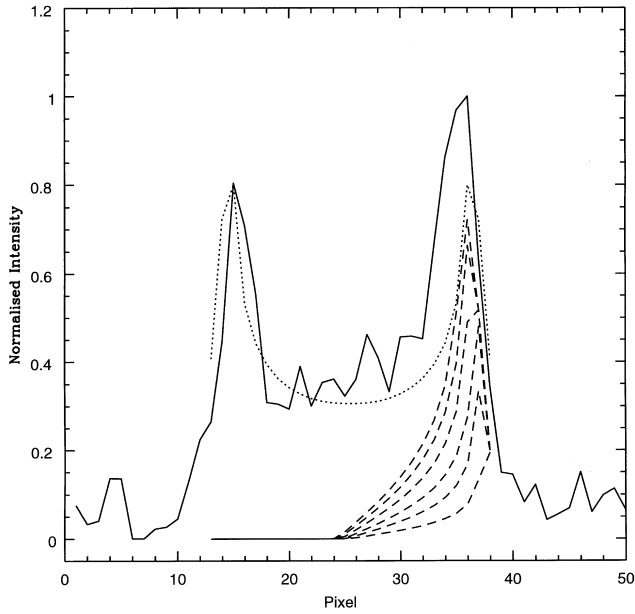


**Figure 8.** Intensity cuts for a cylinder illuminated at angle  $\theta = 10^\circ, 20^\circ, 30^\circ, 45^\circ, 60^\circ$  and  $90^\circ$  (from right to left) to its axis, with viewing angle  $\alpha = 90^\circ$  from the exciting source (dashed lines). The FUV penetrates a distance equal to 20 per cent of the radius along a direction away from the exciting source. Resolution is 8 per cent. Also shown is the form of the cut for isotropic illumination (dotted line), normalized to have the peak intensity as the  $\theta = 90^\circ$  cut, and the data for cut V3 of column II (solid line, see Fig. 4).

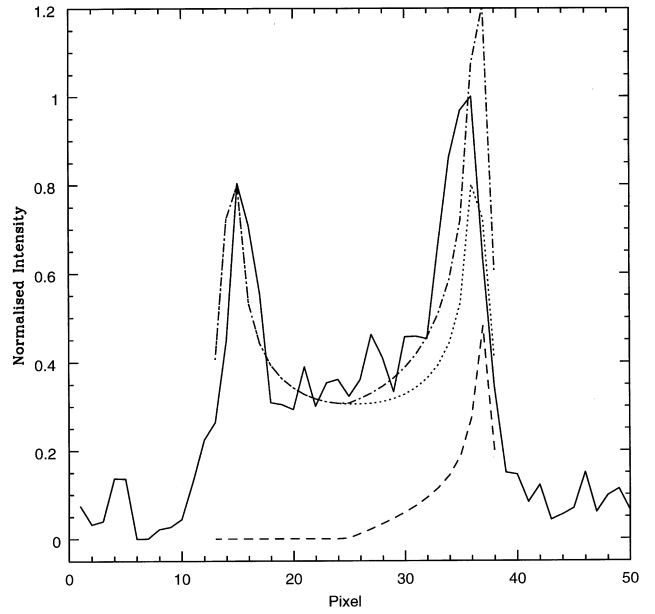


**Figure 9.** 'Best fitted' model overlaid on cut V3 of column II. FUV can penetrate a distance of 20 per cent of the radius from where it enters. Cuts for an isotropic radiation field (dashed line) and one from a star at  $30^\circ$  to the axis (dotted line) are shown, together with their sum (dot-dash line).

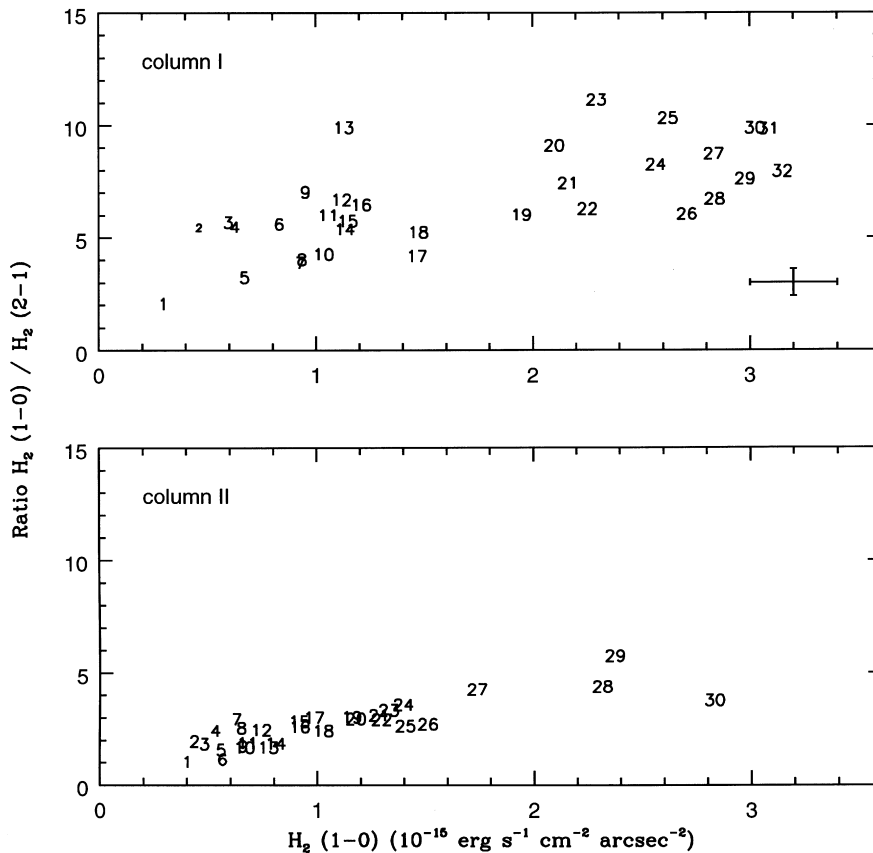


**Figure 10.** Line ratio versus 1–0 line flux, for selected regions in column I (top) and column II (bottom). Typical errors are shown. Symbols are keyed to specific regions in Fig. 11.

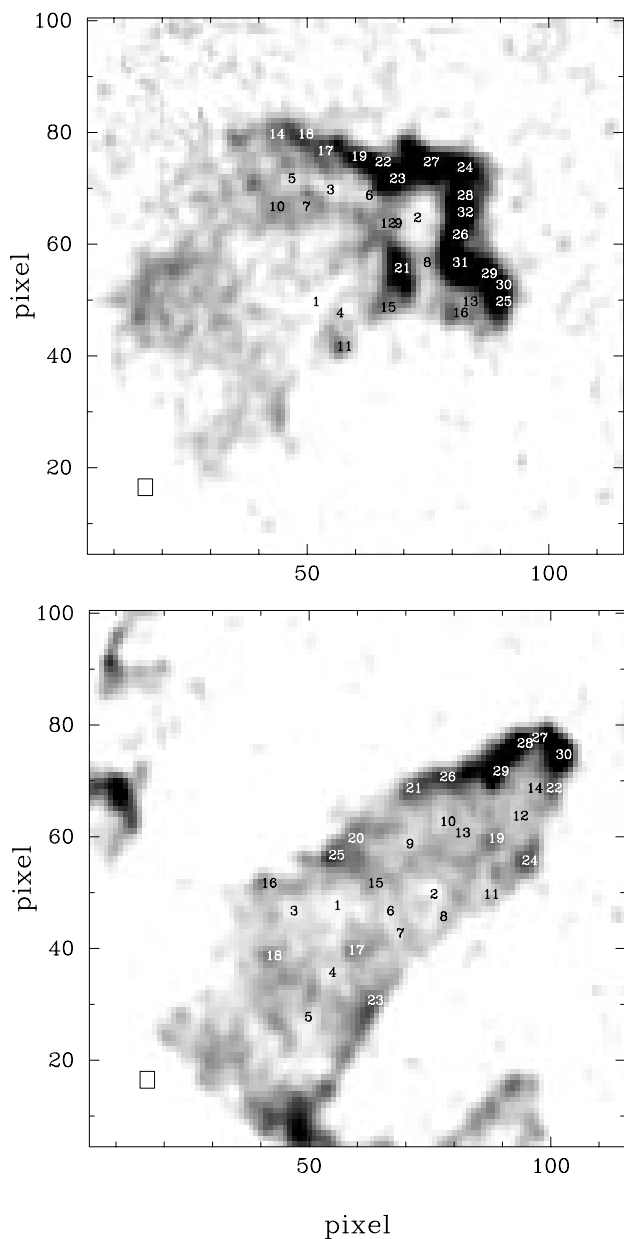


**Figure 11.** Selected regions for which ratios are plotted in Fig. 10, marked on a grey-scale maps of the H<sub>2</sub> 1–0 line emission. For each point shown, a line ratio was formed from the mean of the line emission within a 4 × 4 pixel aperture (as shown in the lower left corner).

fixed 1–0 S(1) line flux, when the proportion of low density gas is highest. It then increases as the number of dense clumps rises along that sightline. For fluxes up to  $\sim 6 \times 10^{-16}$  erg s<sup>-1</sup> cm<sup>-2</sup> arcsec<sup>-2</sup> (the intensity of diffuse emission in a column) the minimum line ratio observed is the pure fluorescent value,  $\sim 2$ . For higher fluxes the minimum ratio rises. This flux is similar to that predicted for average column parameters, discussed at the start of this section ( $n \sim 10^4$  cm<sup>-3</sup>,  $G_0 \sim 10^4$ ,  $f \sim 3$ ), when pure fluorescence occurs.

### 4.3 Time-dependent photodissociation regions

Our discussion in the preceding sections has been predicated on the assumption that the PDR is in a steady state, i.e. the formation of H<sub>2</sub>

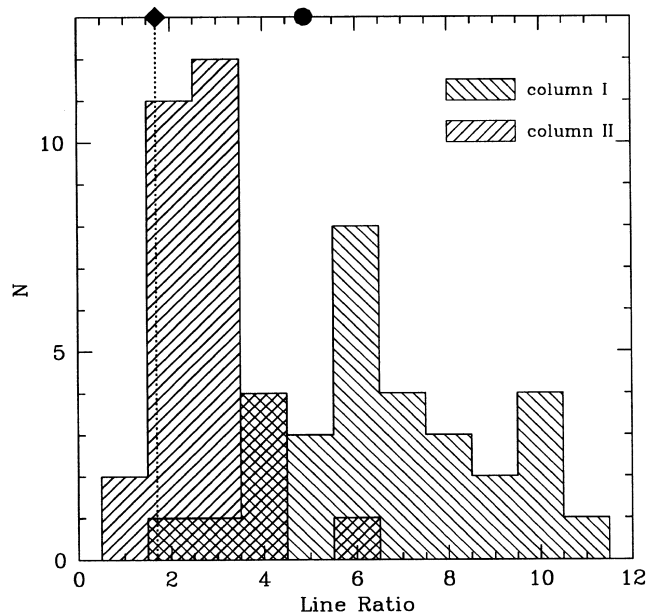


**Figure 12.** Distribution of H<sub>2</sub> (1–0)/(2–1) line ratio in column II (left histogram) and column I (right histogram), computed for the boxes shown in Fig. 11. The dashed vertical line indicates the pure fluorescent ratio of 1.7. Global ratios (total 1–0 flux/total 2–1 flux) are indicated at the top for column I (circle) and column II (diamond).

molecules on dust grains balances their destruction by FUV radiation. However, the time-scale for the H/H<sub>2</sub> dissociation front to reach equilibrium can be long,  $t_{\text{eq}} \sim 5 \times 10^8/n$  yr, compared to time-scales for variation in the field itself (such as a star switching on), or in the density of the gas (e.g. Hollenbach & Natta 1995). The continual exposure of fresh H<sub>2</sub> to the FUV field as the dissociation front moves into a molecular cloud increases the column of fluoresced gas, and thus the line intensities over the equilibrium state.

Bertoldi & Draine (1996) provide a prescription for determining whether a particular PDR may be in equilibrium. It depends on the photoevaporation parameter,  $\psi \sim 5 \times 10^4 S_{49} r_{\text{pc}} / R_{\text{pc}}^2$ , measuring the opacity of the photoevaporation flow to Ly $\alpha$  photons, on the Strömgen parameter,  $\delta \sim 5 \times 10^{-4} / R_{\text{pc}}^2 r_{\text{pc}} n_4^2$ , measuring the dynamical impact of photoevaporation on clumps, and on the ratio  $S_{\text{Ly}\alpha} / S_{\text{FUV}}$  of the number of ionizing photons to FUV photons. Here  $S_{49}$  is the number of ionizing photons/10<sup>49</sup> s<sup>-1</sup>,  $R_{\text{pc}}$  the distance in pc to the exciting star,  $r_{\text{pc}}$  a characteristic size scale for the clumps and  $n_4 = n/10^4$  cm<sup>-3</sup>. For column II we have  $S_{49} \sim 4$ ,  $R_{\text{pc}} \sim 2$ , with  $r_{\text{pc}} \sim 0.1$  and  $n_4 \sim 1$  if we are considering the column as a whole, and  $r_{\text{pc}} \sim 0.01$  and  $n_4 \sim 100$  if we are considering one of the dense clumps inside it. The number of ionizing photons s<sup>-1</sup> at the head of the column is  $\sim 2 \times 10^{46}$  and the number of FUV photons twice this, giving  $S_{\text{Ly}\alpha} / S_{\text{FUV}} \sim 0.5$ . Thus we determine  $\log(\psi) \sim 3.7$ ,  $\log(\delta) \sim -2.3$  for the column, and  $\log(\psi) \sim 2.7$ ,  $\log(\delta) \sim -5.3$  for clumps within it. Comparing with fig. 4(a) of Bertoldi & Draine (1996) suggests that the column itself is not in equilibrium, i.e. the dissociation front is propagating into it too rapidly for equilibrium PDR models to apply. On the other hand, the dense clumps are in marginal equilibrium.

If the PDR is undergoing non-equilibrium photochemistry then we expect elevated H<sub>2</sub> 1–0 S(1) line flux, by an order of magnitude over steady-state predictions (Hollenbach & Natta 1995), and purely fluorescent 1–0/2–1 S(1) line ratios,  $\sim 2$ , as thermal contributions then play a minimal role. However, typical line fluxes

observed within the columns,  $\sim 6 \times 10^{-16} \text{ erg s}^{-1} \text{ cm}^{-2} \text{ arcsec}^{-2}$ , are consistent with steady-state predictions and moreover, the brightest clumps have *elevated* 1–0/2–1 S(1) ratios. Thus, the data suggest that the gas is in photodissociation equilibrium, which, for the conditions within M16, is reached after  $\sim 10^4$  yr. We conclude that the columns have existed and been irradiated by FUV from the central cluster for at least this long if our observations are to be reconciled with the theory for time-dependent PDRs.

## 5 SUMMARY

We have obtained near-infrared line emission images centred on the elephant trunk features in M16. Based on an analysis of H<sub>2</sub> 1–0 S(1), H<sub>2</sub> 2–1 S(1) and Br  $\gamma$  line emission, we find that:

(i) The spatial separation of the H<sub>2</sub> 1–0 and Br  $\gamma$  peaks implies a hydrogen number density of  $n = 2 \times 10^4 \text{ cm}^{-3}$  near the heads of columns I and II.

(ii) Average intensities of the diffuse H<sub>2</sub> 1–0 emission are consistent with PDR theory predictions for pure fluorescence, and are of the order of  $\sim 6 \times 10^{-16} \text{ erg s}^{-1} \text{ cm}^{-2} \text{ arcsec}^{-2}$ . Peak intensities are a factor of  $\sim 5$  higher.

(iii) A simple model for the geometry of the PDR shows that the H<sub>2</sub> 1–0 line emission in the columns is consistent with being excited in cylinders of molecular gas illuminated externally, by a combination of direct and isotropic components.

(iv) The brightest H<sub>2</sub> 1–0 S(1) emission originates from regions that also have elevated 1–0 S(1)/2–1 S(1) line ratios, relative to the purely fluorescent value. This ‘collisional fluorescence’ occurs for a higher fraction of the gas in column I than in column II. We infer gas densities of  $\sim 10^5$  to  $> 10^6 \text{ cm}^{-3}$  for the clumps with elevated ( $> 3$ ) line ratios. Combined, these dense clumps may contain as much molecular mass as the diffuse gas in the columns.

(v) Line intensities are consistent with expectations of steady-state PDR models. In particular, regions with elevated intensities tend to have larger 1–0/2–1 S(1) line ratios, in contradiction to predictions of time-dependent PDR models, in which the most intense regions have pure fluorescent line ratios.

These results were made possible because of the ability of UNSWIRF to provide images with both high spatial and spectral resolution. This study of M16 is one example of how a near-infrared

Fabry-Perot imaging spectrometer such as UNSWIRF can be used effectively to map the internal structure of a PDR.

## ACKNOWLEDGMENTS

We wish to thank the Anglo-Australian Observatory for generous allocations of telescope time, and Y.-S. Sun for valuable assistance calibrating UNSWIRF. We thank Q. Parker and M. Hartley for providing the image in Fig. 1 and J. Hester for providing the image in Fig. 3. LEA and MGB acknowledge the support of the Australian Research Council in funding this research. SDR acknowledges receipt of a UNSW Vice-Chancellor’s Postdoctoral Fellowship. UNSWIRF was also funded by the Australian Research Council. Some of the graphics in this paper were produced using WIP (Morgan 1995).

## REFERENCES

- Allen D. A. et al., 1993, *PASA*, 10, 298  
 Bertoldi F., Draine B. T., 1996, *ApJ*, 458, 222  
 Black J. H., Dalgarno A., 1976, *ApJ*, 203, 132  
 Black J. H., van Dishoeck E. F., 1987, *ApJ*, 322, 412  
 Burton M. G., Brand P. W. J. L., Geballe T. R., Webster A. S., 1989, *MNRAS*, 236, 409.  
 Burton M. G., Hollenbach D. J., Tielens A. G. G. M., 1990, *ApJ*, 365, 620 (BHT)  
 Habing H. J., 1968 *Bull. Astr. Inst. Netherlands*, 19, 421  
 Hester, J. J. et al., 1996, *AJ*, 111, 2349  
 Hillenbrand L. A., Massey P., Strom S. E., Merrill K. M., 1993, *AJ*, 106, 1906  
 Hollenbach D., 1988, *Astro. Lett. and Commun.*, 26, 191  
 Hollenbach D., Natta A., 1995, *ApJ*, 455, 133  
 Hubeny I., Heap S. R., Lanz T., 1998, in Howarth I. D., ed., *ASP Conf. Ser.*, Vol. 131, Boulder–Munich II: Properties of Hot, Luminous Stars. Astron. Soc. Pac., San Francisco, p. 108  
 Morgan J. A. 1995, in Shaw R. A., Payne H. E., Hayes J. J. E., eds. *PASP Conf. Series 77. Astronomical Data Analysis Software and Systems IV*. p. 129  
 Ryder S. D., Allen L. E., Burton M. G., Ashley M. C. B., Storey J. W. V., 1998a, *MNRAS*, 294, 338  
 Ryder S. D., Ashley M. C. B., Sun Y.-S., Burton M. G., Allen L. E., Storey J. W. V., 1998b, *PASA*, 15, 228  
 Tielens A. G. G. M., Hollenbach D. J., 1985, *ApJ*, 291, 722

This paper has been typeset from a T<sub>E</sub>X/L<sup>A</sup>T<sub>E</sub>X file prepared by the author.